THE JOURNAL OF PHYSICAL CHEMISTRY LETTERS
A JOURNAL OF THE AMERICAN CHEMICAL SOCIETY

pubs.acs.org/JPCL

Letter

Femtosecond Exciton and Carrier Relaxation Dynamics of Two-Dimensional (2D) and Quasi-2D Tin Perovskites

Sudhakar Narra, Chia-Yi Lin, Ashank Seetharaman, Efat Jokar, and Eric Wei-Guang Diau*

Cite This: *J. Phys. Chem. Lett.* 2021, 12, 12292−12299

Read Online

ACCESS | Metrics & More | Article Recommendations | Supporting Information

ABSTRACT: The dynamics of exciton and free-carrier relaxation of low-dimensional tin iodide perovskites, $BA_2FA_{n-1}Sn_nI_{3n+1}$, where n = 1 (N1), 2 (N2), 5 (N5), and 10 (N10), were investigated with femtosecond transient absorption spectra (TAS). The absorption and photoluminescence spectra of N1 and N2 show exciton characteristics due to quantum confinement, whereas N5 and N10 display a free-carrier nature, the same as for bulk three-dimensional (3D) films. The TAS profiles were fitted according to a global kinetic model with three time coefficients representing the interactions of biexcitons, trions, and excitons for N1 and N2 and hot carriers, cold carriers, and shallow trap carriers for N5 and N10. The carrier relaxation dynamics of N5 and N10 were similar to those of 3D $FASnI_3$ except for the absence of surface recombination in the deep-trap states due to passivation of the grain surfaces by the long alkyl chain for these quasi-2D samples (N5/N10 vs 3D).

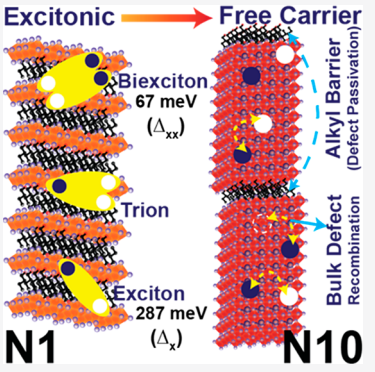

Low-dimensional (LD) organic−inorganic halide perovskites have been broadly utilized in photovoltaic and optoelectronic applications because of their impressive device performance, along with attractive features such as superior atmospheric stability, wavelength tunability, large exciton binding energies, and quantum and dielectric confinement effects.[1−13] They are popularly prepared in the forms of the Ruddlesden−Popper (RP) type,[3,11] the Dion−Jacobson (DJ) type,[5,10] and the alternating cation type[9,11] with molecular formulas of $A'_2A_{n-1}M_nX_{3n+1}$, $A'A_{n-1}M_nX_{3n+1}$, and $A'A_nM_nX_{3n+1}$, respectively. A′ is a bulky organic cation. A is a small organic cation. M represents metal cations such as Sn^{2+} and Pb^{2+}. X represents a halogen atom. They can be mechanically exfoliated into two-dimensional (2D) thin sheet-like structures from their single crystals; multi-quantum-well heterostructures of desired phases can also be formed when they are stacked.[12,13]

The use of LD structures such as 2D and quasi-2D phases in tin perovskite solar cells (PSCs) has proven to be advantageous as they can enhance their stability through passivating the Sn vacancies and suppressing the self-doping due to oxidation of Sn^{2+} to Sn^{4+}, an enduring problem in three-dimensional (3D) Sn PSCs.[1,6,14−16] The reasons for Sn vacancies and self-oxidation of Sn atoms were explained as being due to a strong antibonding coupling between Sn (5s) and I (6p) orbitals, which is weaker in LD structures because orbitals are localized through confinement effects. As a consequence, the overlap between the two orbitals also decreases.[17,18] To obtain the greatest power conversion efficiencies (PCEs) from a 3D Sn PSC, purification of Sn precursors,[19,20] complexation of Sn precursors with dimethyl sulfoxide,[20−22] two-step crystallization,[23,24] additives,[25−28] and mixed cationic structures[29,30] were reported for preparations of Sn perovskite thin-film samples.

Although LD tin perovskites are promising photovoltaic materials, they also suffer from some problems such as random orientation and mixed-phase formation due to rapid nucleation during film preparation.[9,10] A vertical orientation and phase purity are desired characteristics for preparing LD PSCs with optimum performances as they can increase the diffusion length of carriers and enable efficient charge extraction;[7,11,31] on the contrary, random orientations induce asymmetric charge transport, and mixed-phase samples induce energy transfer on a picosecond time scale, with other nonradiative processes. Femtosecond transient absorption spectra (TAS) thus become a powerful tool for identifying the phase purity in LD tin perovskite structures.[14,32] Ultrafast spectral studies on LD lead perovskite films showed the complicated interplay of excitonic, quantum, dielectric confinement effects, and energy-cascade kinetics between LD and higher-dimensional structures,[2,4,8,33,34] but such studies are scarce for tin perovskites.

In this work, we employed a femtosecond TAS technique to study LD Sn perovskite thin-film samples of the type $BA_2FA_{n-1}Sn_nI_{3n+1}$, where BA is n-butyl ammonium, FA is formamidinium, and n = 1 (N1), 2 (N2), 5 (N5), and 10 (N10) according to the stoichiometric ratios of the precursors.

Received: October 19, 2021
Accepted: December 17, 2021
Published: December 21, 2021

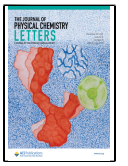

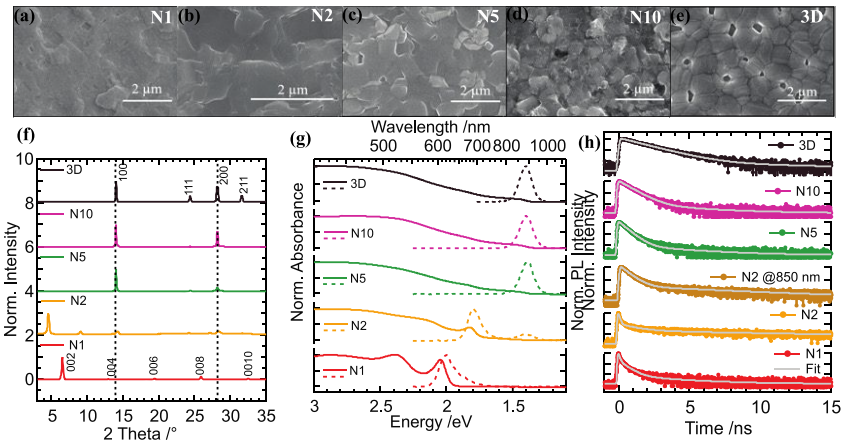

Figure 1. (a–e) SEM images, (f) XRD patterns, (g) ultraviolet–visible (solid lines) and PL (dashed lines) spectra, and (h) TCPSC decay profiles of $BA_2FA_{n-1}Sn_nI_{3n+1}$ (n = 1, 2, 5, 10, and ∞, referring to N1, N2, N5, N10, and 3D, respectively) perovskite thin-film samples.

Here the long ammonium alkyl chain BA served as a spacer (barrier) in a preparation of the LD perovskite thin-film samples. The N1 and N2 samples are shown to be excitonic in nature, whereas the N5 and N10 samples generate free carriers upon excitation; the corresponding kinetic models for relaxation are proposed on the basis of the observed femtosecond TAS results. Our TAS experiments also show evidence for suppression of surface recombination in the LD Sn perovskite thin-film samples reported herein.

The $BA_2FA_{n-1}Sn_nI_{3n+1}$ perovskite thin-film samples were prepared with a one-step spin-coating method as described in the Supporting Information. Structural, morphological, and optical characterizations of the 2D/quasi-2D tin perovskite samples are shown in Figure 1. The scanning electron microscopy (SEM) images (Figure 1a–e) display compact and smooth films for N1, N2, and N5 samples with no grain boundary; N10 and 3D samples show formation of nanograins but also involve pin holes. The GIWAX diffractograms shown in Figure S1a–f indicate that all 2D/quasi-2D samples have random orientations as the Debye–Scherrer rings show discontinuous patterns.[11] The prepared thin films show excellent crystallinity, as one can see from the sharp X-ray diffraction (XRD) signals in Figure 1f. The XRD patterns (Figure 1f) confirm the formation of layered perovskite films; the N1 and N2 samples show signals related to the (00l) (l = 2, 4, 6, 8, and 10) orientation of the 2D perovskites.[35] The N2 sample also showed weak (X00) signals related to the quasi-cubic phase of 3D $FASnI_3$, similar to N5 and N10 samples.[25] In summary, the BA-FA mixed Sn perovskite films prepared in this work had pure 2D, quasi 2D, and pure 3D phases as the FA cation ratio increased from 0% to 100%.

The absorption and photoluminescence (PL) spectra show a marked blue shift with an increase in the proportion of BAI incorporated into Sn perovskite films, as shown in Figure 1g. The PL spectra show a blue shift of 252 nm, from 882 to 630 nm, as the BA ratio increased, which confirms the formation of a LD perovskite phase with a decreasing nanolayer nature. The PL spectrum of N1 shows an asymmetric excitonic band with a maximum at 630 nm; the tail at a longer wavelength is associated with trap states. In contrast, N2 shows two maxima, one prominent at ∼690 nm and the other minor at ∼890 nm. The latter band matches PL bands observed for N5, N10, and 3D PL spectra, which indicates N2, N5, and N10 have a mixed crystal structure containing higher-dimensional phases.

The absorption spectra of Sn perovskite thin-film samples correlate well with their corresponding PL spectra, as shown in Figure 1g. A pure $FASnI_3$ sample shows an absorption edge near 900 nm, whereas a single-layer 2D N1 sample shows a blue shift in its absorption spectrum with a sharp first excitonic absorption band occurring at 606 nm with a Stokes shift of approximately 24 nm (∼0.07 eV) from its first excitonic emission maximum. With this sharp first excitonic transition are also displayed higher excitonic transitions in its absorption spectrum at 430 and 518 nm, corresponding to the second and third excitonic transitions, respectively. The N2 sample shows only one sharp excitonic absorption at 680 nm with a small Stokes shift of 10 nm from its prominent emission maximum. In contrast, for N5 and N10 samples, no excitonic absorption was observed; the spectra resemble that of their 3D analogue. As both N1 and N2 samples show excitonic features, it is desirable to estimate the binding energy of excitons through fitting the steady-state absorption spectra with a well-known quantum-well model, as described elsewhere.[36]

The absorption spectra were fitted according to eqs 1–4:

$$A(E) = c\alpha(E) \tag{1}$$

$$\alpha(E) = X(E) + \mathrm{Con}(E) \tag{2}$$

$$X(E) = \frac{1}{2\eta}\left[\mathrm{erf}\left(\frac{E - E_x}{W_x} - \frac{W_x}{2\eta}\right) + 1\right] \times \exp\left(\frac{W_x^2}{4\eta^2} - \frac{E - E_x}{\eta}\right) \tag{3}$$

$$\mathrm{Con}(E) = \frac{H}{2}\left[\mathrm{erf}\left(\frac{E - E_b - E_x}{W_c}\right) + 1\right] \tag{4}$$

where $X(E)$ and $\mathrm{Con}(E)$ are the absorbances of the exciton and continuum bands, respectively, and E_x, E_b, W_x, W_c, H, and η are the exciton transition energy, exciton binding energy, exciton line width, continuum edge width, continuum edge step height, and asymmetric broadening, respectively. The fitted results are summarized in Table S1. The exciton binding energies of N1 and N2 are 287 and 220 meV, respectively. In contrast, when the 2D layers increased to five (N5), ten (N10), and infinity (3D), the exciton binding energy shows a marked decrease to 10–20 meV, near thermal energy at room

https://doi.org/10.1021/acs.jpclett.1c03427
J. Phys. Chem. Lett. 2021, 12, 12292–12299

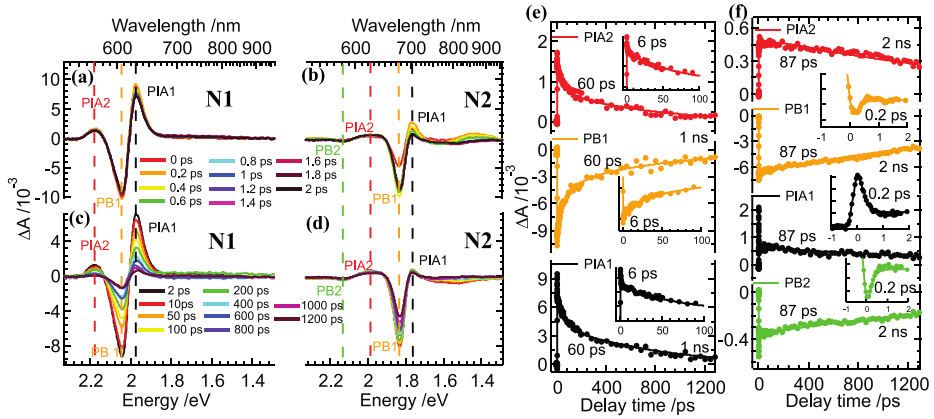

Figure 2. Transient absorption spectra between (a and b) 0−2 ps and (c and d) 2−1200 ps for samples N1 and N2 as indicated. (e and f) Transient absorption profiles of N1 and N2 thin films, respectively. These thin-film samples were excited at 520 nm with a pulse energy of 2.4 μJ cm^{-2}. The transient decay profiles were fitted with a triexponential function model with the resulting time coefficients as indicated.

temperature (~13 meV). This condition would indicate the disappearance of a quantum confinement effect and the fact that the excitons can be dissociated into carriers readily using the thermal energy available at room temperature.

The PL transient decays were observed with time-correlated single-photon counting (TCSPC) to determine the lifetimes of excitons and free carriers in those Sn perovskite samples. For samples N1 and N2, a 375 nm picosecond laser was used for excitation with emission monitored at their respective emission maxima, i.e., at 630 nm (N1) and 690 nm (N2). Alternatively, for the N2 (second phase), N5, N10, and 3D samples, a 635 nm picosecond laser was used for excitation; emission was monitored at 850 nm. The emission decay profiles were fitted with a bi- or triexponential decay function convoluted with the instrument response function (~80 ps); the results are shown in Figure 1h. The fitted results are listed in Table S2. As the number of perovskite layers increased, the average lifetime increased from N1 to N2 but decreased at N5 and then further increased for N10 and 3D. Samples N1 and N2 exhibit an excitonic nature; the increased lifetime is thus an indicator of weakening of the confinement on doubling n from 1 to 2 because excitons recombine much more rapidly than carriers. The decreased lifetime of N5 indicates a poor morphology without distinct grain boundaries. In contrast, the N10 and 3D films showed a systematically increased lifetime. Comparing the N10 and 3D films, we found that N10 shows a morphology that is better than 3D but the carriers are localized in the quasi-2D network, whereas the 3D film shows the crucial role of a 3D network in prolonging the carrier lifetime upon delocalizing charges created in the film. Photovoltaic cells were fabricated with the 2D/quasi-2D Sn perovskite films tested here. $J-V$ curves of the N1−N10 devices are shown in Figure S2. The photocurrent density (J_{SC}), open-circuit voltage (V_{OC}), fill factors (FF), and power conversion efficiencies (PCEs) increase with the thickness of the quantum well. The PCE values for N1, N2, N5, and N10 are 0.1%, 0.7%, 2.1%, and 4% respectively, which are lower than those for 3D or 3D/2D Sn perovskites. V_{OC} of N1 is larger than for other samples because of a large band gap, whereas N2 showed a smaller V_{OC} because of its mixed-phase feature. The insight into the mechanism of exciton/carrier relaxation in these samples was further investigated with the femtosecond TAS technique.

Femtosecond TAS experiments with the N1 and N2 samples were performed with excitation at 520 nm and a probe in the range of 530−970 nm; the time-dependent spectra are shown in panels a−d of Figure 2, with the corresponding temporal profiles depicted in panels e and f of Figure 2. Both N1 and N2 samples display a sharp photobleach (PB1) band corresponding to their first excitonic transitions at 605 and 676 nm, respectively, with photoinduced absorption (PIA) bands on either side of the PB1 band labeled PIA1 and PIA2 for longer and shorter wavelength sidebands, respectively. The N2 sample shows an additional PB band (PB2) on the short wavelength side, corresponding to a higher excitonic transition, and broad PIA and PB bands in the near-IR region due to the existence of high-order phases. As spectral features of N1 and N2 samples closely resemble 2D quantum-well structures with sharp excitonic resonances in their steady-state spectra, photoexcitation is expected to lead to weakening of confinement of the excitons produced. In a strongly confined system, photoexcitation induces an increase in the bandgap due to a decrease in the exciton binding energy, whereas in a weakly confined system, a decrease in the bandgap is observed due to the effect of bandgap renormalization (BGR).[37,38] Apart from reduction of the exciton binding energy and the BGR effect leading to the spectral shifts, carrier−carrier scattering and exciton localization at interfaces lead to spectral broadening.[38,39] The actual shape of the TA spectra depends on the cumulative effects of all of the aforementioned processes. As both N1 and N2 samples show a second-derivative feature with an intense PIA band on the red side of the TAS, these samples might fall under a weak confinement regime, with sample N1 showing a PIA1 band that is more intense than that of sample N2. The weak confinement can also be rationalized from the perspective of inherent p-doping of the valence bands of Sn perovskites due to the possible Sn^{2+}/Sn^{4+} oxidation process. In the case of Pb-halide perovskite systems, PIA bands displayed spin effects and these PIA bands were assigned to biexcitonic and polaronic excitonic states.[39−42] According to the circular polarization experiments, the PIA1 band of the Pb-halide quantum wells was assigned to a biexcitonic state[42] populated by the probe pulse. In our case, a similar circular polarization experiment was performed to show the biexciton nature of the PIA1 band for the N1 sample (Figure S3). The PIA2 band could be a polaronic excitonic state populated through photoexcitation by breaking of the inversion symmetry of the inorganic layer due to structural distortion similar to the Pb-halide perovskites.[39]

https://doi.org/10.1021/acs.jpclett.1c03427
J. Phys. Chem. Lett. 2021, 12, 12292−12299

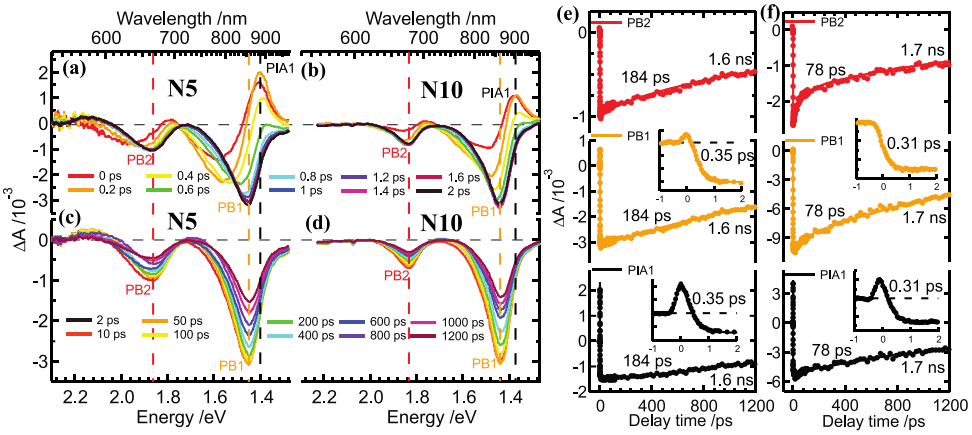

Figure 3. Transient absorption spectra between (a and b) 0−2 ps and (c and d) 2−1200 ps for samples N5 and N10 as indicated. (e and f) Transient absorption profiles of N5 and N10 thin films, respectively. The thin-film samples were excited at 520 nm with a pulse energy of 2.4 μJ cm^{-2}. ΔA values of TA spectra of N10 were scaled relative to N5 for the sake of clarity; the actual magnitudes are shown in their TA decay profiles. The transient decay profiles were fitted with a consecutive model with a triexponential function with fitted time coefficients as indicated.

To strengthen the assignment of the PIA band to the biexcitonic state, resonant excitation experiments (λ_{ex} = 600 nm) have been performed further as the yield of biexcitons decreases under resonant conditions when compared with that for above bandgap excitation conditions. Experiments at a resonant excitation wavelength (λ_{ex} = 600 nm) performed for a pure N1 sample shown in Figure S4 display clear isosbestic points between PB and PIA bands, implying that these excitonic states are coupled near band edge reflecting the BGR effect, whereas excitation at a shorter wavelength (λ_{ex} = 520 nm) shows collapsed isosbestic points at greater delays, which implies that the origin of these bands differs slightly. The intensity of band PIA1 is smaller under resonant conditions than with excitation at shorter wavelengths as the yield of biexcitons is typically smaller under resonant conditions. Thus, the intensity variations displayed by the PIA1 band from both circular polarization and resonant excitation experiments suggest the PIA1 band with origins in both BGR and biexcitonic states.

A triexponential kinetic model of satisfactory quality was applied to fit the TAS transients with convolution of a Gaussian pulse (~250 fs) to the decay profiles of PB and PIA bands for both samples N1 and N2. For sample N1, the fitted results show the following time coefficients: τ_1 = 6 ps, τ_2 = 60 ps, and $\tau_3 \sim$ 1 ns. Similarly, for sample N2, the fitted results show the following time coefficients: τ_1 = 200 fs, τ_2 = 87 ps, and $\tau_3 \sim$ 2 ns. τ_1 of N2 is, remarkably, much smaller than that of N1, which is discussed below. Although the origin of PIA bands differs from that of PB bands, their unified decay suggests the correlated or coupled nature of the electronic states; decoupling such states requires further study. A similar unified decay between PB and PIA bands was observed in Pb-halide perovskite quantum wells reported elsewhere.[43] The time coefficients τ_1−τ_3 obtained from fitting the transient kinetics were assigned to recombinations mediated by biexcitons, trions, and excitons, respectively, as explained below. The biexciton's Auger recombination typically occurs in several picoseconds in perovskite nanocrystals,[36] and the observed time scale matches the time coefficient τ_1 reported for N1 here; thus, τ_1 should be that of annihilation of excitons via biexciton formation. The slower decay τ_2 is often associated with recovery of excitons via formation of trions in perovskite nanocrystals due to the presence of surface defects and ionized impurities, but their existence has not been considered so far for 2D perovskite quantum-well structures. We propose that formation of trions in N1 and N2 is more likely because of the p-doping of the valence bands due to oxidation of Sn^{2+} to Sn^{4+}; the decay component τ_2 should be that of a trion, whereas the nanosecond decay component τ_3 should be that of an exciton.

The TA spectra of samples N5 and N10 in Figure 3 show a close resemblance to the 3D $FASnI_3$ results reported,[44] also shown in Figure S5. It might be possible that both N5 and N10 also formed impure higher-dimension phases similar to N2. Both samples N5 and N10 show two PB bands and one PIA band, assigned to PB1, PB2, and PIA1, as indicated in Figure 3. The magnitudes of ΔA of sample N10 were >3 times those of sample N5, as one can see from the magnitudes of PB1 bands shown in their respective decay profiles. The PB1 band is associated with a band edge bleaching signal, whereas PIA1 is associated with hot carriers undergoing cooling to form cold carriers. These samples also show a characteristic bandgap renormalization in the earlier period between 0 and 2 ps (see panels a and b of Figure 3) similar to the 3D Sn perovskite.[44] As the TAS profiles are similar to those of the 3D $FASnI_3$, their relaxation kinetic model was also treated similarly using a parallel sequential approach to account for surface and bulk trap-mediated recombination dynamics,[44] but this model failed to fit the transient data globally. In contrast with 3D $FASnI_3$, the transients of samples N5 and N10 follow only a consecutive relaxation kinetic model according to eq 5:

$$\text{hot carriers} \xrightarrow{\tau_1} \text{cold carriers} \xrightarrow{\tau_2} \text{trap states} \xrightarrow{\tau_3} \text{ground state} \quad (5)$$

The global fit of the transient decay data according to the consecutive model described in eq 5 yielded decay time coefficients associated with hot-carrier cooling (τ_1), trap-state filling (τ_2), and bulk trap-state-mediated recombination (τ_3), giving values of 355 fs, 184 ps, and 1.6 ns, respectively, for sample N5. Similarly, for N10, the consecutive model yielded time coefficients of 304 fs, 78 ps, and 1.7 ns, respectively. The decay profiles and curve fits of the transients are shown in panels e and f of Figure 3; their corresponding spectra from a global fit are shown in Figure S6. The trap-state filling from cold carriers (τ_2) relaxes more rapidly for N10 than for N5, but ΔA for N5 is smaller than for N10 because of the weaker absorption (Figure S7) of the former. Furthermore, the fit of

https://doi.org/10.1021/acs.jpclett.1c03427
J. Phys. Chem. Lett. 2021, 12, 12292−12299

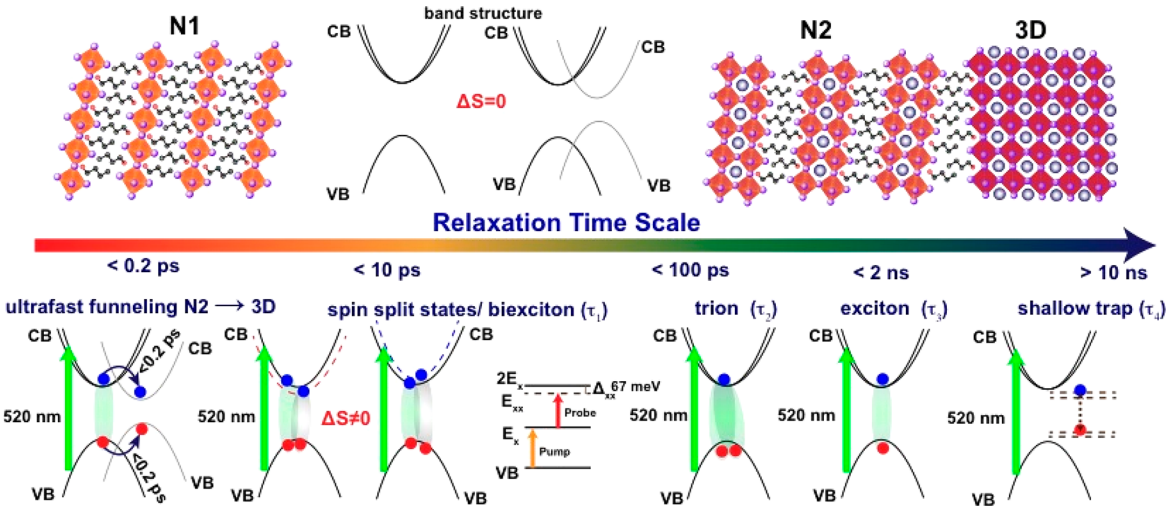

Figure 4. Structural representation and mechanism of exciton-mediated relaxation of samples N1 and N2. Gray curves represent high-order (or 3D) phases; dashed curves represent spin-split states.

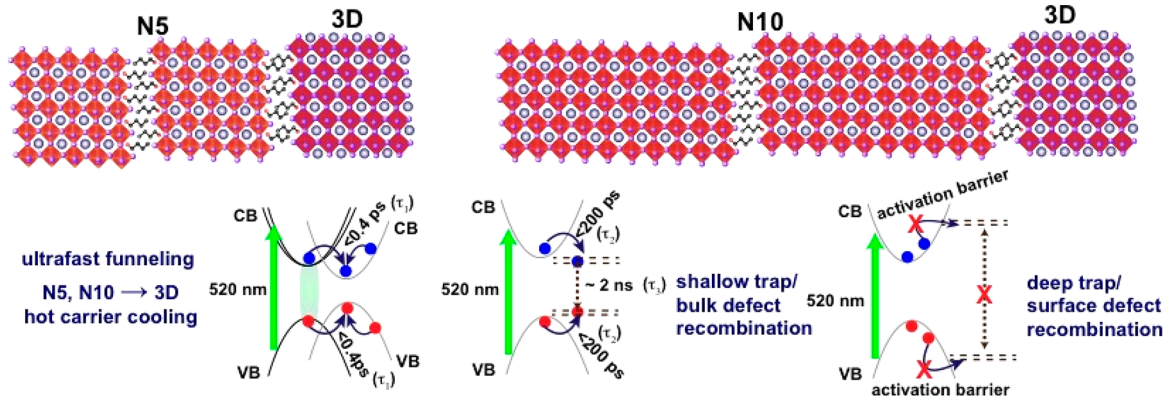

Figure 5. Structural representation and mechanism of free-carrier-mediated relaxation of samples N5 and N10. Dashed lines represent shallow- and deep-trap states as indicated.

sample N5 and N10 transients with a consecutive model indicates that the surface defect relaxation is absent in these samples, because the films show fewer grain boundaries than their 3D analogue shown in the SEM images (panels c and d of Figure 1vs panel e of Figure 1). The absence of surface recombination is a remarkable feature of these samples; the underlying reasons are discussed below.

On the basis of the TAS results shown in Figures 2 and 3, we propose an exciton/carrier relaxation mechanism for samples N1, N2, N5, and N10, which is shown in Figure 4 and Figure 5. LD perovskites with a short quantum well such as samples N1 and N2 behave like excitons, whereas N5 and N10 behave like free carriers. The relaxation mechanism of N1 and N2 shown in Figure 4 can explain the transient decays associated with biexcitons, trions, excitons, and shallow traps for observed time coefficients τ_1−τ_4, respectively; τ_1−τ_3 were determined by TAS, and τ_4 was determined by TCSPC. The two PIA bands were observed on the blue and red sides of the PB band in the form of populating of dark excitons following photoexcitation due to symmetry breaking ($\Delta S \neq 0$), whereas the biexcitonic state is formed when the dark exciton encounters a bright exciton, which decays rapidly on a subpicosecond time scale with time coefficient τ_1. The binding energy of a biexciton of N1 determined from the energy difference between PB1 and PIA bands is ∼67 meV, which is consistent with the biexciton binding energies determined for the LD Pb perovskites.[36,45] Similarly, when an exciton interacts with a free carrier or ionized impurity, a trion species is formed, which decays on a picosecond time scale with time coefficient τ_2; direct recombination occurs on a nanosecond time scale with time coefficient τ_3. To compare the relaxation dynamics between N1 and N2, the most pronounced difference is a biexcitonic interconversion between bright and dark excitons. τ_1 of N2 is much smaller than that of N1 (200 fs vs 6 ps), presumably because of the retarded interaction of the latter by the BA ligand. Recent theoretical calculations indicate funneling of electrons and holes in the so-called insulating-barrier layers for LD Pb perovskite quantum-well structures.[45] The formation of LD Sn perovskite biexcitons in different layers of sample N1 is thus plausible,[46] which retards the lifetimes of the biexcitons for N1 because of the insulating barrier layer. In sample N2, however, most bright and dark excitons might be located nearby in the same layer to induce a rapid biexcitonic relaxation. We cannot, however, exclude the existence of phase impurity in sample N2 that accelerated the biexcitonic relaxation. The time scale of energy transfer in mixed-phase LD Pb perovskites was determined to be <0.2 ps.[33,47−49] Beyond the rapid spin-split biexciton relaxation, accelerated relaxation of biexciton in the case of N2 involving a high-order phase transformation hence seems to be possible.

https://doi.org/10.1021/acs.jpclett.1c03427
J. Phys. Chem. Lett. 2021, 12, 12292−12299

The carrier relaxation mechanism of samples N5 and N10 shown in Figure 5 is similar to that of 3D $FASnI_3$ reported elsewhere,[44] except that these LD samples show no surface defect relaxation. Similar to N2, samples N5 and N10 might involve a high-order phase transformation to occur too rapidly to be observed within our apparatus response. The carrier relaxation model in Figure 5 shows the consecutive decay processes involving ultrarapid hot-carrier relaxation (and possibly funneling to the high-order or 3D phase), trap-state filling, and bulk defect-mediated recombination with time coefficients $\tau_1-\tau_3$ occurring on subpicosecond, picosecond, and nanosecond time scales, respectively. The absence of deeply trapped surface recombination in the LD samples compared with 3D $FASnI_3$ can be understood in terms of an increased activation barrier to populate the deep defect states located inside the conduction band. Time-dependent density functional theory calculations indicate that LUMO levels of the A-site cation lie above the conduction band minima acting as carrier traps for perovskite materials.[50] A-Site cation blending with additives such as $EDAI_2$[25] and co-cations such as guanidinium,[30] azetidinium,[29] and phenylhydrazinium thiocyanate[51] show passivation effects with enhanced carrier lifetimes. The effect of surface passivation might induce shifting of LUMO levels of hybridized organic cations, which can scavenge surface charge carriers. Our result shows that the BA chain could also afford an effect similar to that of additives and co-cations on creating an activation barrier for charge trapping on the surface of the LD tin perovskite so that the deeply trapped surface states cannot be reached (Figure 5). The TAS decays presented here show that surface recombination can be retarded with bulky alkyl chains, whereas the TCSPC decay kinetics (τ_4) show a carrier lifetime longer for 3D $FASnI_3$ than for LD structures. Passivating the surface with an appropriate long alkyl chain would thus yield LD tin perovskite samples with the desired optical characteristics.

In conclusion, we employed a femtosecond TAS technique to study the relaxation dynamics of low-dimensional (LD) Sn perovskites ($BA_2FA_{n-1}Sn_nI_{3n+1}$) in a series fabricated using butyl ammonium iodide (BAI) as a terminating reagent to cut the 3D network into 2D and quasi-2D quantum-well structures. Investigations of SEM, XRD, GIWAX, ultraviolet−visible, and PL spectra were undertaken to support the formation of LD structures according to varied stoichiometric ratios of precursors for samples N1 (n = 1), N2 (n = 2), N5 (n = 5), and N10 (n = 10). The absorption spectra were fitted to a quantum-well model to determine binding energies of 287, 220, 21, and 10 meV for N1, N2, N5, and N10, respectively. These results indicate that N1 and N2 samples are excitonic but N5 and N10 are free carriers in nature. The PL decay profiles measured with TCSPC show increased lifetimes as n increases, with the slow decay component assigned to be the shallow trap-state recombination on a time scale greater than nanoseconds. The TAS profiles measured for N1 and N2 show an excitonic behavior. Their subsequent decay dynamics were fitted with a triexponential function kinetic model involving formation of biexcitons, tri-ions, and excitons in these LD samples. The TAS profiles of N5 and N10 resemble those of 3D $FASnI_3$, but their recombination dynamics can be described with a consecutive decay model without a contribution from the surface trap states due to the involvement of the bulky BA chains to suppress the carrier recombination on the surface. The lifetimes of excitons are much shorter than the lifetimes of carriers, which is consistent with the corresponding order of device performance: N10 > N5 > N2 > N1. Our results hence disclose a comprehensive concept for LD tin perovskites with long-chain ligands to suppress surface recombination caused by trap states to enhance the device performance.

■ ASSOCIATED CONTENT

Supporting Information

The Supporting Information is available free of charge at https://pubs.acs.org/doi/10.1021/acs.jpclett.1c03427.

Experimental Methods, Figures S1−S6, and Tables S1 and S2 (PDF)

■ AUTHOR INFORMATION

Corresponding Author

Eric Wei-Guang Diau − *Department of Applied Chemistry and Institute of Molecular Science, National Yang Ming Chiao Tung University, Hsinchu 30010, Taiwan; Center for Emergent Functional Matter Science, National Yang Ming Chiao Tung University, Hsinchu 30010, Taiwan;* orcid.org/0000-0001-6113-5679; Email: diau@mail.nctu.edu.tw

Authors

Sudhakar Narra − *Department of Applied Chemistry and Institute of Molecular Science, National Yang Ming Chiao Tung University, Hsinchu 30010, Taiwan; Center for Emergent Functional Matter Science, National Yang Ming Chiao Tung University, Hsinchu 30010, Taiwan;* orcid.org/0000-0003-4893-9204

Chia-Yi Lin − *Department of Applied Chemistry and Institute of Molecular Science, National Yang Ming Chiao Tung University, Hsinchu 30010, Taiwan*

Ashank Seetharaman − *Department of Applied Chemistry and Institute of Molecular Science, National Yang Ming Chiao Tung University, Hsinchu 30010, Taiwan*

Efat Jokar − *Department of Applied Chemistry and Institute of Molecular Science, National Yang Ming Chiao Tung University, Hsinchu 30010, Taiwan; Center for Emergent Functional Matter Science, National Yang Ming Chiao Tung University, Hsinchu 30010, Taiwan*

Complete contact information is available at: https://pubs.acs.org/10.1021/acs.jpclett.1c03427

Notes

The authors declare no competing financial interest.

■ ACKNOWLEDGMENTS

The Taiwan Ministry of Science and Technology (MOST 110-2123-M-A49-001 and MOST 110-2634-F-009-026) and the Center for Emergent Functional Matter Science of National Yang Ming Chiao Tung University (NYCU) from The Featured Areas Research Center Program within the framework of the Higher Education Sprout Project by Taiwan Ministry of Education (MOE) supported this research. The National Synchrotron Radiation Research Center (NSRRC), Hsinchu, Taiwan, provided beam time for measurements of GIWAX.

■ REFERENCES

(1) Chen, G.; Li, P.; Xue, T.; Su, M.; Ma, J.; Zhang, Y.; Wu, T.; Han, L.; Aldamasy, M.; Li, M.; Li, Z.; Ma, J.; Chen, S.; Zhao, Y.; Wang, F.;

Song, Y. Design of Low Bandgap $CsPb_{1-x}Sn_xI_2Br$ Perovskite Solar Cells with Excellent Phase Stability. *Small* **2021**, *17*, 2101380.
(2) Mauck, C. M.; Tisdale, W. A. Excitons in 2D Organic−Inorganic Halide Perovskites. *Trends Chem.* **2019**, *1*, 380−393.
(3) Park, I.; Chu, L.; Leng, K.; Choy, Y. F.; Liu, W.; Abdelwahab, I.; Zhu, Z.; Ma, Z.; Chen, W.; Xu, Q.; Eda, G.; Loh, K. P. Highly Stable Two-Dimensional Tin(II) Iodide Hybrid Organic−Inorganic Perovskite Based on Stilbene Derivative. *Adv. Funct. Mater.* **2019**, *29*, 1904810.
(4) Deng, S.; Shi, E.; Yuan, L.; Jin, L.; Dou, L.; Huang, L. Long-Range Exciton Transport and Slow Annihilation in Two-Dimensional Hybrid Perovskites. *Nat. Commun.* **2020**, *11*, 664.
(5) Li, P.; Liu, X.; Zhang, Y.; Liang, C.; Chen, G.; Li, F.; Su, M.; Xing, G.; Tao, X.; Song, Y. Low-Dimensional Dion−Jacobson-Phase Lead-Free Perovskites for High-Performance Photovoltaics with Improved Stability. *Angew. Chem., Int. Ed.* **2020**, *59*, 6909−6914.
(6) Grancini, G.; Roldán-Carmona, C.; Zimmermann, I.; Mosconi, E.; Lee, X.; Martineau, D.; Narbey, S.; Oswald, F.; De Angelis, F.; Graetzel, M.; Nazeeruddin, M. K. One-Year Stable Perovskite Solar Cells by 2D/3D Interface Engineering. *Nat. Commun.* **2017**, *8*, 15684.
(7) Zhao, Z.; Gu, F.; Wang, C.; Zhan, G.; Zheng, N.; Bian, Z.; Liu, Z. Orientation Regulation of Photoactive Layer in Tin-Based Perovskite Solar Cells with Allylammonium Cations. *Sol. RRL.* **2020**, *4*, 2000315.
(8) Katan, C.; Mercier, N.; Even, J. Quantum and Dielectric Confinement Effects in Lower-Dimensional Hybrid Perovskite Semiconductors. *Chem. Rev.* **2019**, *119*, 3140−3192.
(9) Liu, P.; Yu, S.; Xiao, S. Research Progress on Two-Dimensional (2D) Halide Organic−Inorganic Hybrid Perovskites. *Sustain. Energy Fuels* **2021**, *5*, 3950−3978.
(10) Li, X.; Hoffman, J. M.; Kanatzidis, M. G. The 2D Halide Perovskite Rulebook: How the Spacer Influences Everything from the Structure to Optoelectronic Device Efficiency. *Chem. Rev.* **2021**, *121*, 2230−2291.
(11) Liao, Y.; Liu, H.; Zhou, W.; Yang, D.; Shang, Y.; Shi, Z.; Li, B.; Jiang, X.; Zhang, L.; Quan, L. N.; Quintero-Bermudez, R.; Sutherland, B. R.; Mi, Q.; Sargent, E. H.; Ning, Z. Highly-Oriented Low-Dimensional Tin Halide Perovskites with Enhanced Stability and Photovoltaic Performance. *J. Am. Chem. Soc.* **2017**, *139*, 6693−6699.
(12) Li, J.; Wang, J.; Zhang, Y.; Wang, H.; Lin, G.; Xiong, X.; Zhou, W.; Luo, H.; Li, D. Fabrication of Single Phase 2D Homologous Perovskite Microplates by Mechanical Exfoliation. *2D Mater.* **2018**, *5*, 021001.
(13) Wang, K.; Park, J. Y.; Akriti; Dou, L. Two-dimensional Halide Perovskite Quantum-well Emitters: A Critical Review. *EcoMat* **2021**, *3*, No. e12104.
(14) Jokar, E.; Cheng, P.-Y.; Lin, C.-Y.; Narra, S.; Shahbazi, S.; Diau, E. W.-G. Enhanced Performance and Stability of 3D/2D Tin Perovskite Solar Cells Fabricated with a Sequential Solution Deposition. *ACS Energy Lett.* **2021**, *6*, 485−492.
(15) Lin, Y.; Bai, Y.; Fang, Y.; Chen, Z.; Yang, S.; Zheng, X.; Tang, S.; Liu, Y.; Zhao, J.; Huang, J. Enhanced Thermal Stability in Perovskite Solar Cells by Assembling 2D/3D Stacking Structures. *J. Phys. Chem. Lett.* **2018**, *9*, 654−658.
(16) Yu, B.; Chen, Z.; Zhu, Y.; Wang, Y.; Han, B.; Chen, G.; Zhang, X.; Du, Z.; He, Z. Heterogeneous 2D/3D Tin-Halides Perovskite Solar Cells with Certified Conversion Efficiency Breaking 14%. *Adv. Mater.* **2021**, *33*, 2102055.
(17) Zhang, T.; Sun, Q.; Zhang, X.; Shen, Y.; Wang, M. Minimizing Energy Loss in Two-Dimensional Tin Halide Perovskite Solar Cells—A Perspective. *APL Mater.* **2021**, *9*, 020906.
(18) Hoye, R. L. Z.; Hidalgo, J.; Jagt, R. A.; Correa-Baena, J.; Fix, T.; MacManus-Driscoll, J. L. The Role of Dimensionality on the Optoelectronic Properties of Oxide and Halide Perovskites, and Their Halide Derivatives. *Adv. Energy Mater.* **2021**, 2100499.
(19) Nakamura, T.; Yakumaru, S.; Truong, M. A.; Kim, K.; Liu, J.; Hu, S.; Otsuka, K.; Hashimoto, R.; Murdey, R.; Sasamori, T.; Kim, H. D.; Ohkita, H.; Handa, T.; Kanemitsu, Y.; Wakamiya, A. Sn(IV)-Free Tin Perovskite Films Realized by in Situ Sn(0) Nanoparticle Treatment of the Precursor Solution. *Nat. Commun.* **2020**, *11*, 3008.
(20) Ozaki, M.; Katsuki, Y.; Liu, J.; Handa, T.; Nishikubo, R.; Yakumaru, S.; Hashikawa, Y.; Murata, Y.; Saito, T.; Shimakawa, Y.; Kanemitsu, Y.; Saeki, A.; Wakamiya, A. Solvent-Coordinated Tin Halide Complexes as Purified Precursors for Tin-Based Perovskites. *ACS Omega* **2017**, *2*, 7016−7021.
(21) Hao, F.; Stoumpos, C. C.; Guo, P.; Zhou, N.; Marks, T. J.; Chang, R. P. H.; Kanatzidis, M. G. Solvent-Mediated Crystallization of $CH_3NH_3SnI_3$ Films for Heterojunction Depleted Perovskite Solar Cells. *J. Am. Chem. Soc.* **2015**, *137*, 11445−11452.
(22) Cao, D. H.; Stoumpos, C. C.; Yokoyama, T.; Logsdon, J. L.; Song, T.-B.; Farha, O. K.; Wasielewski, M. R.; Hupp, J. T.; Kanatzidis, M. G. Thin Films and Solar Cells Based on Semiconducting Two-Dimensional Ruddlesden−Popper $(CH_3(CH_2)_3NH_3)_2(CH_3NH_3)_{n-1}Sn_nI_{3n+1}$ Perovskites. *ACS Energy Lett.* **2017**, *2*, 982−990.
(23) Shahbazi, S.; Li, M.-Y.; Fathi, A.; Diau, E. W.-G. Realizing a Cosolvent System for Stable Tin-Based Perovskite Solar Cells Using a Two-Step Deposition Approach. *ACS Energy Lett.* **2020**, *5*, 2508−2511.
(24) Song, D.; Narra, S.; Li, M.-Y.; Lin, J.-S.; Diau, E. W.-G. Interfacial Engineering with a Hole-Selective Self-Assembled Monolayer for Tin Perovskite Solar Cells via a Two-Step Fabrication. *ACS Energy Lett.* **2021**, *6*, 4179−4186.
(25) Jokar, E.; Chien, C.-H.; Fathi, A.; Rameez, M.; Chang, Y.-H.; Diau, E. W.-G. Slow Surface Passivation and Crystal Relaxation with Additives to Improve Device Performance and Durability for Tin-Based Perovskite Solar Cells. *Energy Environ. Sci.* **2018**, *11*, 2353−2362.
(26) Diau, E. W.-G.; Jokar, E.; Rameez, M. Strategies To Improve Performance and Stability for Tin-Based Perovskite Solar Cells. *ACS Energy Lett.* **2019**, *4*, 1930−1937.
(27) Horn, J.; Scholz, M.; Oum, K.; Lenzer, T.; Schlettwein, D. Influence of Phenylethylammonium Iodide as Additive in the Formamidinium Tin Iodide Perovskite on Interfacial Characteristics and Charge Carrier Dynamics. *APL Mater.* **2019**, *7*, 031112.
(28) Milot, R. L.; Klug, M. T.; Davies, C. L.; Wang, Z.; Kraus, H.; Snaith, H. J.; Johnston, M. B.; Herz, L. M. The Effects of Doping Density and Temperature on the Optoelectronic Properties of Formamidinium Tin Triiodide Thin Films. *Adv. Mater.* **2018**, *30*, 1804506.
(29) Jokar, E.; Hou, P. H.; Bhosale, S. S.; Chuang, H. S.; Narra, S.; Diau, E. W.-G. Mixing of Azetidinium in Formamidinium Tin Triiodo Perovskite Solar Cells for Enhanced Photovoltaic Performance and High Stability in Air. *ChemSusChem* **2021**, *14*, 4415−4421.
(30) Jokar, E.; Chien, C.; Tsai, C.; Fathi, A.; Diau, E. W.-G. Robust Tin-Based Perovskite Solar Cells with Hybrid Organic Cations to Attain Efficiency Approaching 10%. *Adv. Mater.* **2019**, *31*, 1804835.
(31) Sirbu, D.; Balogun, F. H.; Milot, R. L.; Docampo, P. Layered Perovskites in Solar Cells: Structure, Optoelectronic Properties, and Device Design. *Adv. Energy. Mater.* **2021**, *11*, 2003877.
(32) Fathi, A.; Jokar, E.; Lee, Y.-P.; Diau, E. W.-G. A Direct Mapping Approach to Understand Carrier Relaxation Dynamics in Varied Regions of a Polycrystalline Perovskite Film. *Angew. Chem., Int. Ed.* **2020**, *59*, 19001−19005.
(33) Proppe, A. H.; Elkins, M. H.; Voznyy, O.; Pensack, R. D.; Zapata, F.; Besteiro, L. V.; Quan, L. N.; Quintero-Bermudez, R.; Todorovic, P.; Kelley, S. O.; Govorov, A. O.; Gray, S. K.; Infante, I.; Sargent, E. H.; Scholes, G. D. Spectrally Resolved Ultrafast Exciton Transfer in Mixed Perovskite Quantum Wells. *J. Phys. Chem. Lett.* **2019**, *10*, 419−426.
(34) Cho, J.; DuBose, J. T.; Kamat, P. V. Charge Carrier Recombination Dynamics of Two-Dimensional Lead Halide Perovskites. *J. Phys. Chem. Lett.* **2020**, *11*, 2570−2576.
(35) Wang, Z.; Wang, F.; Zhao, B.; Qu, S.; Hayat, T.; Alsaedi, A.; Sui, L.; Yuan, K.; Zhang, J.; Wei, Z.; Tan, Z. Efficient Two-Dimensional Tin Halide Perovskite Light-Emitting Diodes via a

https://doi.org/10.1021/acs.jpclett.1c03427
J. Phys. Chem. Lett. 2021, 12, 12292−12299

Spacer Cation Substitution Strategy. *J. Phys. Chem. Lett.* **2020**, *11*, 1120−1127.
(36) Vale, B. R. C.; Socie, E.; Burgos-Caminal, A.; Bettini, J.; Schiavon, M. A.; Moser, J.-E. Exciton, Biexciton, and Hot Exciton Dynamics in CsPbBr3 Colloidal Nanoplatelets. *J. Phys. Chem. Lett.* **2020**, *11*, 387−394.
(37) Wu, X.; Trinh, M. T.; Zhu, X.-Y. Excitonic Many-Body Interactions in Two-Dimensional Lead Iodide Perovskite Quantum Wells. *J. Phys. Chem. C* **2015**, *119*, 14714−14721.
(38) Miller, A.; Riblet, P.; Mazilu, M.; White, S.; Holden, T. M.; Cameron, A. R.; Perozzo, P. Exciton Saturation in GaAs Multiple Quantum Wells at Room Temperature. *J. Appl. Phys.* **1999**, *86*, 3734−3744.
(39) Rossi, D.; Wang, H.; Dong, Y.; Qiao, T.; Qian, X.; Son, D. H. Light-Induced Activation of Forbidden Exciton Transition in Strongly Confined Perovskite Quantum Dots. *ACS Nano* **2018**, *12*, 12436−12443.
(40) Giovanni, D.; Chong, W. K.; Liu, Y. Y. F.; Dewi, H. A.; Yin, T.; Lekina, Y.; Shen, Z. X.; Mathews, N.; Gan, C. K.; Sum, T. C. Coherent Spin and Quasiparticle Dynamics in Solution-Processed Layered 2D Lead Halide Perovskites. *Adv. Sci.* **2018**, *5*, 1800664.
(41) McKechnie, S.; Frost, J. M.; Pashov, D.; Azarhoosh, P.; Walsh, A.; Van Schilfgaarde, M. Dynamic Symmetry Breaking and Spin Splitting in Metal Halide Perovskites. *Phys. Rev. B: Condens. Matter. Mater. Phys.* **2018**, *98*, 085108.
(42) Chen, X.; Lu, H.; Wang, K.; Zhai, Y.; Lunin, V.; Sercel, P. C.; Beard, M. C. Tuning Spin-Polarized Lifetime in Two-Dimensional Metal−Halide Perovskite through Exciton Binding Energy. *J. Am. Chem. Soc.* **2021**, *143*, 19438−19445.
(43) Cheng, B.; Li, T.-Y.; Maity, P.; Wei, P.-C.; Nordlund, D.; Ho, K.-T.; Lien, D.-H.; Lin, C.-H.; Liang, R.-Z.; Miao, X.; Ajia, I. A.; Yin, J.; Sokaras, D.; Javey, A.; Roqan, I. S.; Mohammed, O. F.; He, J.-H. Extremely Reduced Dielectric Confinement in Two-Dimensional Hybrid Perovskites with Large Polar Organics. *Commun. Phys.* **2018**, *1*, 80.
(44) Narra, S.; Jokar, E.; Pearce, O.; Lin, C.-Y.; Fathi, A.; Diau, E. W.-G. Femtosecond Transient Absorption Spectra and Dynamics of Carrier Relaxation of Tin Perovskites in the Absence and Presence of Additives. *J. Phys. Chem. Lett.* **2020**, *11*, 5699−5704.
(45) Yu, B.; Zhang, C.; Chen, L.; Qin, Z.; Huang, X.; Wang, X.; Xiao, M. Ultrafast Dynamics of Photoexcited Carriers in Perovskite Semiconductor Nanocrystals. *Nanophotonics* **2021**, *10*, 1943−1965.
(46) Giovanni, D.; Ramesh, S.; Righetto, M.; Lim, J. W. M.; Zhang, Q.; Wang, Y.; Ye, S.; Xu, Q.; Mathews, N.; Sum, T. C. The Physics of Interlayer Exciton Delocalization in Ruddlesden−Popper Lead Halide Perovskites. *Nano Lett.* **2021**, *21*, 405−413.
(47) Magdaleno, A. J.; Seitz, M.; Frising, M.; Herranz de la Cruz, A.; Fernández-Domínguez, A. I.; Prins, F. Efficient Interlayer Exciton Transport in Two-Dimensional Metal-Halide Perovskites. *Mater. Horiz.* **2021**, *8*, 639−644.
(48) Elkins, M. H.; Pensack, R.; Proppe, A. H.; Voznyy, O.; Quan, L. N.; Kelley, S. O.; Sargent, E. H.; Scholes, G. D. Biexciton Resonances Reveal Exciton Localization in Stacked Perovskite Quantum Wells. *J. Phys. Chem. Lett.* **2017**, *8*, 3895−3901.
(49) Bouduban, M. E. F.; Burgos-Caminal, A.; Ossola, R.; Teuscher, J.; Moser, J.-E. Energy and Charge Transfer Cascade in Methylammonium Lead Bromide Perovskite Nanoparticle Aggregates. *Chem. Sci.* **2017**, *8*, 4371−4380.
(50) Lee, Y.; Kim, H.; Hong, K.-H.; Cho, K. Femtosecond Quantum Dynamics of Excited-State Evolution of Halide Perovskites: Quantum Chaos of Molecular Cations. *J. Phys. Chem. C* **2021**, *125*, 10676−10684.
(51) Jokar, E.; Chuang, H.-S.; Kuan, C.-H.; Wu, H.-P.; Hou, C.-H.; Shyue, J.-J.; Diau, E. W.-G. Slow Passivation and Inverted Hysteresis for Hybrid Tin Perovskite Solar Cells Attaining 13.5% via Sequential Deposition. *J. Phys. Chem. Lett.* **2021**, *12*, 10106−10111.

https://doi.org/10.1021/acs.jpclett.1c03427
J. Phys. Chem. Lett. 2021, 12, 12292−12299